A High-Order-Accurate 3D Surface Integral Equation Solver for Uniaxial Anisotropic Media

Jin Hu[®], Graduate Student Member, IEEE, and Constantine Sideris[®], Member, IEEE

Abstract—This article introduces a high-order accurate surface integral equation (SIE) method for solving 3-D electromagnetic scattering for dielectric objects with uniaxially anisotropic permittivity tensors. The N-Müller formulation is leveraged, resulting in a second-kind integral formulation, and a finitedifference (FD)-based approach is used to deal with the strongly singular terms resulting from the dyadic Green's functions for uniaxially anisotropic media while maintaining the high-order accuracy of the discretization strategy. The integral operators are discretized via a Nyström-collocation approach, which represents the unknown surface densities in terms of Chebyshev polynomials on curvilinear quadrilateral surface patches. The convergence is investigated for various geometries, including a sphere, cube, a complicated non-uniform rational basis spline (NURBS) geometry imported from a 3-D computer-aided design (CAD) modeler software, and a nanophotonic silicon waveguide, and the results are compared against a commercial finite-element (FE) solver. To the best of our knowledge, this is the first demonstration of high-order accuracy for objects with uniaxially anisotropic materials using SIEs.

Index Terms—High-order accuracy, integral equations. N-Müller formulation, scattering, spectral methods.

I. INTRODUCTION

SURFACE integral equations (SIEs) are a powerful approach for numerically solving Maxwell's equations and have been applied to solve a plethora of scattering problems, including antennas [1], radar scattering [2], and most recently nanophotonics [3], [4], [5]. Traditionally known as open boundary problems due to satisfying the Sommerfeld radiation condition by design, SIEs have also recently been successfully applied for solving dielectric waveguiding problems, which require simulating waveguides extending to and from infinity, in both two [3], [6] and three [5] dimensions. Unlike other volumetric computational approaches, such as finite-difference (FD) and finite-element (FE) methods, which require generating complicated volume meshes, SIE methods only mesh the surfaces between material regions. Since SIE methods

Manuscript received 7 March 2022; revised 19 January 2023; accepted 4 February 2023. Date of publication 23 February 2023; date of current version 5 May 2023. This work was supported in part by the Air Force Office of Scientific Research under Grant FA9550-20-1-0087, and in part by the National Science Foundation under Grant CCF-1849965 and Grant CCF-2047433. (Corresponding author: Constantine Sideris.)

The authors are with the Department of Electrical and Computer Engineering, University of Southern California, Los Angeles, CA 90089 USA (e-mail: jinhu@usc.edu; csideris@usc.edu).

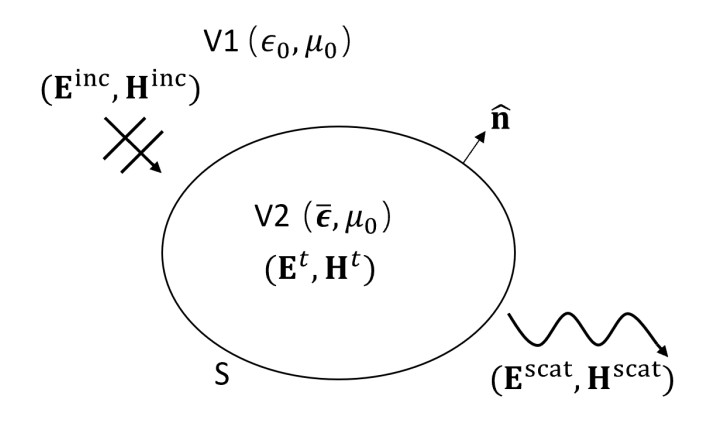
Color versions of one or more figures in this article are available at https://doi.org/10.1109/TAP.2023.3246084.

Digital Object Identifier 10.1109/TAP.2023.3246084

solve for unknowns over surface rather than volume meshes. they may also result in significantly smaller problems compared with using volumetric approaches in scenarios with high volume to surface area ratios. SIEs have predominantly been used for solving problems with homogeneous, isotropic dielectrics due to the availability of closed-form dyadic Green's functions, which can be readily discretized using suitable numerical quadrature and singularity treatment approaches. For example, our recent work in [7] demonstrates high-order convergence discretizing the magnetic field integral equation (MFIE) and the N-Müller formulation for modeling metals and dielectrics, respectively, using a Chebyshevbased Nyström method. On the other hand, many anisotropic materials are commonly used in engineering applications, such as anisotropic dielectric substrates for antennas [8], [9] and liquid crystal claddings for designing reconfigurable nanophotonic devices [10]. However, despite the fact that closed-form Green's functions have been derived for uniaxially anisotropic media, there is a dearth of work available using SIE methods to solve problems with these materials. In fact, the only discretization approaches in the literature are [11], [12], [13], [14], and [15], which present compelling results comparing against volumetric methods but do not report on error or convergence properties.

Indeed, although closed form expressions for the dyadic Green's functions for materials with uniaxially anisotropic permittivity and permeability do exist [16], they are significantly more complex and challenging to discretize than the corresponding expressions for the isotropic material case [see (24)]. The Poggio-Miller-Chang-Harrington-Wu-Tsai (PMCHWT) [17], [18], [19] formulation is used in [11] and discretized using the method of moments (MoM) and RWG basis functions [20], [21]. The strongly singular part of the G_{ee} operator (known as the T operator in the literature for the isotropic case) is dealt with in the usual manner by using integration by parts to decrease the kernel singularity by moving a derivative to the testing function. However, the $\overline{\mathbf{G}}_{em} \propto (\nabla \times \overline{\mathbf{G}}_{ee})$ operator (known as the K operator in the literature for the isotropic case) also contains a strong singularity, which cannot be easily reduced. Mumcu et al. [11] approximate integrals with $\overline{\mathbf{G}}_{em}$ by shifting the target point r slightly off the surface. Unfortunately, this approach is expected to result in poor accuracy, since the operator is evaluated on a different target point than the original intended one on the surface, and, furthermore, because

0018-926X © 2023 IEEE. Personal use is permitted, but republication/redistribution requires IEEE permission. See https://www.ieee.org/publications/rights/index.html for more information.



Electromagnetic scattering from a uniaxial anisotropic object illuminated by an incident wave excitation.

the kernel remains nearly singular and is, therefore, very challenging to numerically integrate even with the target point being shifted off the surface. Follow-on work has extended the approach in [11] to a preconditioned single-source formulation [15], high-order MoM [13], [14], and has accelerated it using adaptive cross approximation (ACA) [12], although these works all still use the same low-accuracy approach to deal with the singularity and do not show convergence results.

In this work, we present a new discretization strategy, which when combined with the singular integration approach using Chebhyshev polynomials to represent the unknown densities introduced in [7] achieves the high-order accuracy for scattering from objects composed of uniaxially anisotropic materials. To the best of our knowledge, this is the very first demonstration of a boundary integral solver for anisotropic media, which achieves the high-order accuracy. Note that in all of our examples, we assume that only the permittivity tensor is anisotropic and that $\mu_r = 1$; however, the approach presented can readily be extended to support materials with both permittivity and permeability tensors having anisotropy. This article is organized as follows. Section II briefly introduces the surface integral formulation under consideration for dielectric scatterers. Section III reviews the dyadic Green's functions for uniaxial anisotropic media and sets up a system of integral equations for a scenario with an anisotropic scatterer inside an isotropic exterior medium based on the N-Müller formulation. Section IV analyzes the singular behavior of each anisotropic kernel operator. Section V presents our Chebyshev-based discretization and singular integration approach for accurate evaluation of the integral operators. Finally, Section VI demonstrates error convergence and both near and far-field numerical results for four different example cases.

II. SIE FORMULATION

We consider the problem of evaluating the scattered field from a nonmagnetic uniaxial anisotropic object (V_2) embedded in a free space region (V_1) , as shown in Fig. 1. Note that for the subsequent derivations, we assume V_1 is free space without loss of generality; however, it can also be any arbitrary isotropic homogeneous background medium. The object is illuminated by an incident field excitation (\mathbf{E}^{inc} , \mathbf{H}^{inc}) that will lead to both scattered fields (\mathbf{E}^{scat} , \mathbf{H}^{scat}) outside the object and transmitted fields $(\mathbf{E}^t, \mathbf{H}^t)$ inside the object.

To obtain an equivalent problem for the exterior region based on surface equivalence principle, the interior fields can be nulled, and the total fields in the exterior region $(\mathbf{E}_1, \mathbf{H}_1)$ are a superposition of incident and scattered fields, which can be represented as follows:

$$\mathbf{E}_{1}(\mathbf{r}) = \mathbf{E}^{\text{inc}}(\mathbf{r}) + \int_{S} \overline{\mathbf{G}}_{em}^{1}(\mathbf{r}, \mathbf{r}') \cdot \mathbf{M}_{1}(\mathbf{r}') d\sigma(\mathbf{r}') + \int_{S} \overline{\mathbf{G}}_{ee}^{1}(\mathbf{r}, \mathbf{r}') \cdot \mathbf{J}_{1}(\mathbf{r}') d\sigma(\mathbf{r}')$$
(1)

$$\mathbf{H}_{1}(\mathbf{r}) = \mathbf{H}^{\text{inc}}(\mathbf{r}) + \int_{S} \overline{\mathbf{G}}_{mm}^{1}(\mathbf{r}, \mathbf{r}') \cdot \mathbf{M}_{1}(\mathbf{r}') d\sigma(\mathbf{r}') + \int_{S} \overline{\mathbf{G}}_{me}^{1}(\mathbf{r}, \mathbf{r}') \cdot \mathbf{J}_{1}(\mathbf{r}') d\sigma(\mathbf{r}')$$
(2)

 $\mathbf{J}_1 = \hat{n} \times \mathbf{H}_1$ and $\mathbf{M}_1 = \mathbf{E}_1 \times \hat{n}$ are the equivalent surface electric and magnetic current densities for the exterior region. $\overline{\mathbf{G}}_{ee}^1$ and $\overline{\mathbf{G}}_{em}^1$ (resp. $\overline{\mathbf{G}}_{me}^1$ and $\overline{\mathbf{G}}_{mm}^1$) are the dyadic Green's functions of the exterior region, corresponding to the electric fields (respectively, magnetic fields) produced by delta electric and magnetic current sources, respectively, in V_1 . By letting the target point **r** approach the surface S from the exterior V_1 and taking the cross products of (1) and (2) with the unit normal vector to the surface \hat{n} , the first set of equations is obtained as follows:

$$\frac{1}{2}\mathbf{M}_{1} + \mathcal{K}_{em}^{1}\mathbf{M}_{1} + \mathcal{K}_{ee}^{1}\mathbf{J}_{1} = -\hat{n} \times \mathbf{E}^{\text{inc}}$$

$$\frac{1}{2}\mathbf{J}_{1} - \mathcal{K}_{mm}^{1}\mathbf{M}_{1} - \mathcal{K}_{me}^{1}\mathbf{J}_{1} = \hat{n} \times \mathbf{H}^{\text{inc}}$$
(4)

$$\frac{1}{2}\mathbf{J}_{1} - \mathcal{K}_{mm}^{1}\mathbf{M}_{1} - \mathcal{K}_{me}^{1}\mathbf{J}_{1} = \hat{n} \times \mathbf{H}^{\text{inc}}$$
 (4)

$$\mathcal{K}_{\alpha\beta}^{1}[\mathbf{a}](\mathbf{r}) = \hat{n}(\mathbf{r}) \times \int_{S} \overline{\mathbf{G}}_{\alpha\beta}^{1}(\mathbf{r}, \mathbf{r}') \cdot \mathbf{a}(\mathbf{r}') d\sigma(\mathbf{r}') \quad \mathbf{r} \in S \quad (5)$$

where the subscripts α and β can be either e or m. Similarly, the equivalent problem for the interior region can be formulated by setting the exterior field to zero, allowing the total fields inside the anisotropic uniaxial region $(\mathbf{E}_2, \mathbf{H}_2)$, which are the same as the transmitted fields, to be represented as follows:

$$\mathbf{E}_{2}(\mathbf{r}) = \int_{S} \overline{\mathbf{G}}_{em}^{2}(\mathbf{r}, \mathbf{r}') \cdot \mathbf{M}_{2}(\mathbf{r}') d\sigma(\mathbf{r}')$$

$$+ \int_{S} \overline{\mathbf{G}}_{ee}^{2}(\mathbf{r}, \mathbf{r}') \cdot \mathbf{J}_{2}(\mathbf{r}') d\sigma(\mathbf{r}') \qquad (6)$$

$$\mathbf{H}_{2}(\mathbf{r}) = \int_{S} \overline{\mathbf{G}}_{mm}^{2}(\mathbf{r}, \mathbf{r}') \cdot \mathbf{M}_{2}(\mathbf{r}') d\sigma(\mathbf{r}')$$

$$+ \int_{S} \overline{\mathbf{G}}_{me}^{2}(\mathbf{r}, \mathbf{r}') \cdot \mathbf{J}_{2}(\mathbf{r}') d\sigma(\mathbf{r}'). \qquad (7)$$

Analogous to the exterior problem, $\mathbf{J}_2 = (-\hat{n}) \times \mathbf{H}_2$ and $\mathbf{M}_2 = \mathbf{E}_2 \times (-\hat{n})$ are the equivalent surface electric and magnetic current densities for the interior problem, and $\overline{\mathbf{G}}_{ee}^2$ $\overline{\mathbf{G}}_{em}^2$, $\overline{\mathbf{G}}_{me}^2$, and $\overline{\mathbf{G}}_{mm}^2$ are the four dyadic Green's functions for the internal anisotropic uniaxial region V_2 for which the subscripts can be interpreted in the same manner as the exterior functions described above. By letting the target point r

approach surface S from the interior V_2 and taking the cross products of (6) and (7) with the surface normal vector \hat{n} , the second set of equations is obtained

$$\frac{1}{2}\mathbf{M}_2 - \mathcal{K}_{em}^2 \mathbf{M}_2 - \mathcal{K}_{ee}^2 \mathbf{J}_2 = \mathbf{0}$$
 (8)

$$\frac{1}{2}\mathbf{J}_2 + \mathcal{K}_{mm}^2 \mathbf{M}_2 + \mathcal{K}_{me}^2 \mathbf{J}_2 = \mathbf{0}$$
 (9)

with the integral operator $\mathcal{K}^2_{\alpha\beta}(\alpha, \beta \in \{e, m\})$ defined the same way as in (5), except superscript "2" now indicates the uniaxially anisotropic interior region V_2 .

Note that due to the tangential continuity conditions of the fields across the boundary, we must have that

$$J = J_1 = -J_2, \quad M = M_1 = -M_2,$$
 (10)

which leaves two remaining unknowns J and M and four equations. As is commonly done, the four equations can be reduced to two via linear combination

$$\alpha_1(3) + \alpha_2(8)$$

 $\beta_1(4) + \beta_2(9)$ (11)

which is the system of integral equations that is used in our formulation. After the equivalent surface densities J and M have been solved, the total fields outside and inside the uniaxial object can be determined anywhere by evaluating the representation formulas (1) and (2), and (6) and (7), respectively. The specific choice of coefficients α and β and the explicit form of each dyadic Green's function will be explained in Section III.

III. DYADIC GREEN'S FUNCTIONS FOR UNIAXIAL ANISOTROPIC MEDIA

The interior region V_2 in the formulation is filled with a uniaxially anisotropic dielectric, which can characterized by the relative permittivity tensor

$$\overline{\epsilon} = \epsilon_{\perp} \overline{\mathbf{I}} + (\epsilon_{\parallel} - \epsilon_{\perp}) \hat{\mathbf{c}} \hat{\mathbf{c}}$$
 (12)

where $\hat{\mathbf{c}}$ is a unit vector parallel to the distinguished axis, ϵ_{\parallel} is the relative permittivity along the direction of $\hat{\mathbf{c}}$, ϵ_{\perp} is the relative permittivity along the directions perpendicular to $\hat{\mathbf{c}}$, and $\bar{\mathbf{I}}$ represents the unit dyadic. It has been shown in [11] and [16] that closed-form expressions exist for the dyadic Green's functions for this type of material, which we reproduce here for completeness

$$\overline{\mathbf{G}}_{ee}^{2} = \frac{i\omega\mu_{0}}{4\pi} \left\{ \frac{\nabla\nabla}{\mathbf{k}_{\perp}^{2}} \frac{e^{i\mathbf{k}_{\perp}\mathbf{R}_{e}}}{\mathbf{R}_{e}} + \epsilon_{\parallel} \frac{e^{i\mathbf{k}_{\perp}\mathbf{R}_{e}}}{\mathbf{R}_{e}} \overline{\boldsymbol{\epsilon}}^{-1} - \left[\frac{\epsilon_{\parallel}e^{i\mathbf{k}_{\perp}\mathbf{R}_{e}}}{\epsilon_{\perp}\mathbf{R}_{e}} - \frac{e^{i\mathbf{k}_{\perp}\mathbf{R}}}{\mathbf{R}} \right] \left[\frac{(\mathbf{R} \times \hat{\mathbf{c}})(\mathbf{R} \times \hat{\mathbf{c}})}{(\mathbf{R} \times \hat{\mathbf{c}})^{2}} \right] - \left[\frac{\epsilon_{\parallel} - \epsilon_{\perp}}{\epsilon_{\perp}} \frac{e^{i\mathbf{k}_{\perp}(\mathbf{R}_{e} + \mathbf{R})/2}}{\mathbf{R}_{e} + \mathbf{R}} \frac{\sin(\mathbf{k}_{\perp}(\mathbf{R}_{e} - \mathbf{R})/2)}{(\mathbf{k}_{\perp}(\mathbf{R}_{e} - \mathbf{R})/2)} \right] \times \left[\overline{\mathbf{I}} - \hat{\mathbf{c}}\hat{\mathbf{c}} - 2 \frac{(\mathbf{R} \times \hat{\mathbf{c}})(\mathbf{R} \times \hat{\mathbf{c}})}{(\mathbf{R} \times \hat{\mathbf{c}})^{2}} \right] \right\}$$

$$\overline{\mathbf{G}}_{mm}^{2} = \frac{i\omega\epsilon_{0}}{4\pi} \left\{ \frac{\nabla\nabla}{\mathbf{k}_{0}^{2}} \frac{e^{i\mathbf{k}_{\perp}\mathbf{R}}}{\mathbf{R}} + \epsilon_{\perp} \frac{e^{i\mathbf{k}_{\perp}\mathbf{R}}}{\mathbf{R}} \overline{\mathbf{I}} \right\}$$
(13)

$$+ \left[\frac{\epsilon_{\parallel} e^{i\mathbf{k}_{\perp} \mathbf{R}_{e}}}{\mathbf{R}_{e}} - \frac{\epsilon_{\perp} e^{i\mathbf{k}_{\perp} \mathbf{R}}}{\mathbf{R}} \right] \left[\frac{(\mathbf{R} \times \hat{\mathbf{c}})(\mathbf{R} \times \hat{\mathbf{c}})}{(\mathbf{R} \times \hat{\mathbf{c}})^{2}} \right]$$

$$+ \left[(\epsilon_{\parallel} - \epsilon_{\perp}) \frac{e^{i\mathbf{k}_{\perp} (\mathbf{R}_{e} + \mathbf{R})/2}}{\mathbf{R}_{e} + \mathbf{R}} \frac{\sin(\mathbf{k}_{\perp} (\mathbf{R}_{e} - \mathbf{R})/2)}{(\mathbf{k}_{\perp} (\mathbf{R}_{e} - \mathbf{R})/2)} \right]$$

$$\times \left[\overline{\mathbf{I}} - \hat{\mathbf{c}} \hat{\mathbf{c}} - 2 \frac{(\mathbf{R} \times \hat{\mathbf{c}})(\mathbf{R} \times \hat{\mathbf{c}})}{(\mathbf{R} \times \hat{\mathbf{c}})^{2}} \right]$$

$$(14)$$

$$\overline{\mathbf{G}}_{em}^{2} = \frac{i}{\omega \epsilon_{0}} \overline{\epsilon}^{-1} \cdot \nabla \times \overline{\mathbf{G}}_{mm}^{2} \tag{15}$$

$$\overline{\mathbf{G}}_{me}^{2} = \frac{1}{i\omega\mu_{0}}\nabla\times\overline{\mathbf{G}}_{ee}^{2} \tag{16}$$

where ϵ_0 and μ_0 are the permittivity and permeability of free space, respectively, ω is the angular frequency of the incident field, $\mathbf{k}_0 = \omega \sqrt{\epsilon_0 \mu_0}$ is the wavenumber in free space, $\mathbf{R} = \mathbf{r} - \mathbf{r}'$ and $\mathbf{R} = |\mathbf{R}|$ are the relative position vector and the distance, respectively, from a source point to an observation point, $\overline{\boldsymbol{\epsilon}}^{-1} = \boldsymbol{\epsilon}_{\perp}^{-1} \overline{\mathbf{I}} + (\boldsymbol{\epsilon}_{\parallel}^{-1} - \boldsymbol{\epsilon}_{\perp}^{-1}) \hat{\mathbf{c}} \hat{\mathbf{c}}$ is the inverse of $\overline{\boldsymbol{\epsilon}}$, and \mathbf{R}_e and \mathbf{k}_{\perp} are given by

$$R_{e} = \sqrt{\epsilon_{\parallel} (\mathbf{R} \cdot \overline{\epsilon}^{-1} \cdot \mathbf{R})}, \quad \mathbf{k}_{\perp} = \mathbf{k}_{0} \sqrt{\epsilon_{\perp}}.$$
 (17)

Note that if the permittivity tensor is set to $\bar{\epsilon} = \bar{\mathbf{I}}$, the above uniaxially anisotropic Green's functions simplify to the well-known isotropic dyadic Green's functions for free space

$$\overline{\mathbf{G}}_{ee}^{1} = \frac{i\omega\mu_{0}}{4\pi} \left[\frac{\nabla\nabla}{\mathbf{k}_{0}^{2}} \frac{e^{i\mathbf{k}_{0}\mathbf{R}}}{\mathbf{R}} + \frac{e^{i\mathbf{k}_{0}\mathbf{R}}}{\mathbf{R}} \overline{\mathbf{I}} \right]$$
(18)

$$\overline{\mathbf{G}}_{mm}^{1} = \frac{i\omega\epsilon_{0}}{4\pi} \left[\frac{\nabla\nabla}{\mathbf{k}_{0}^{2}} \frac{e^{i\mathbf{k}_{0}\mathbf{R}}}{\mathbf{R}} + \frac{e^{i\mathbf{k}_{0}\mathbf{R}}}{\mathbf{R}} \overline{\mathbf{I}} \right]$$
(19)

$$\overline{\mathbf{G}}_{em}^{1} = \frac{i}{\omega \epsilon_{0}} \nabla \times \overline{\mathbf{G}}_{mm}^{1} \tag{20}$$

$$\overline{\mathbf{G}}_{me}^{1} = \frac{1}{i\omega\mu_{0}} \nabla \times \overline{\mathbf{G}}_{ee}^{1}.$$
 (21)

The linear combination coefficients in the integral equation system (11) are chosen according to the N-Müller formulation to be: $\alpha_1 = \epsilon_{r1} = 1$, $\alpha_2 = \epsilon_{r2} = \epsilon_{\perp}$, and $\beta_1 = \mu_{r1} = \beta_2 = \mu_{r2} = 1$. Although the hypersingular part of the $\overline{\mathbf{G}}_{ee}^1$ and $\overline{\mathbf{G}}_{ee}^2$ operator does not fully cancel each other out as in the isotropic case [22] due to the directional dependence of the gradient of the anisotropic Green's function, this formulation is still expected to result in a well-conditioned system due to its second-kind nature. Table I reports the number of iterations required for generalized minimum residual method (GMRES) to converge for a number of test cases. The resulting integral equations can be represented in matrix form as follows:

$$\begin{bmatrix} \mathcal{K}_{em}^{1} - \epsilon_{\perp} \mathcal{K}_{em}^{2} + \frac{1+\epsilon_{\perp}}{2} \mathcal{I} & \mathcal{K}_{ee}^{1} - \epsilon_{\perp} \mathcal{K}_{ee}^{2} \\ \mathcal{K}_{mm}^{2} - \mathcal{K}_{mm}^{1} & \mathcal{K}_{me}^{2} - \mathcal{K}_{me}^{1} + \mathcal{I} \end{bmatrix} \begin{bmatrix} \mathbf{M} \\ \mathbf{J} \end{bmatrix} \\ = \begin{bmatrix} -\hat{n} \times \mathbf{E}^{\text{inc}} \\ \hat{n} \times \mathbf{H}^{\text{inc}} \end{bmatrix}$$
(22)

where \mathcal{I} is the identity operator, and the expressions for dyadic Green's functions $\overline{\mathbf{G}}_{\alpha\beta}^{i}$ involved in each of the integral operators $\mathcal{K}_{\alpha\beta}^{i}(i \in \{1, 2\}; \alpha, \beta \in \{e, m\})$ are given by (13)–(16) and (18)–(21).

TABLE I

Number of GMRES Iterations Versus Total Number of Unknowns Q With the Relative Residual Error Tolerance 10^{-3} for Various Geometry and Permittivity Settings

Q	cube $(\epsilon_{\perp} =$	sphere $(\epsilon_{\perp} =$	sphere $(\epsilon_{\perp} =$
	$10, \epsilon_{ } = 20)$	$10, \epsilon_{ } = 20)$	$2, \epsilon_{ } = 20)$
11616	288	91	279
13824	288	86	143
16224	288	83	74
18816	288	80	60
21600	288	77	46
24576	288	74	45
27744	289	71	45
31104	289	68	45

IV. SINGULARITY ANALYSIS OF INTEGRAL OPERATORS

In order to evaluate the action of each of the integral operators $\mathcal{K}^i_{\alpha\beta}$ on the densities with high accuracy, care must be taken to analyze and properly handle the singular behavior of each operator.

A. Singularity of \mathcal{K}_{qq}^2

At first glance, the \mathcal{K}^i_{ee} and $\mathcal{K}^i_{mm}(i \in \{1,2\})$ operators appear to both be hypersingular with $O(1/R^3)$ singularities due to the $\nabla \nabla$ operator acting on a term with O(1/R) singularity. However, vector identities can be utilized to transfer the one of the ∇ operators to the density term, and the other ∇ , which can be made to not depend on the source integration coordinate, can be pulled outside of the integral. For example, taking the \mathcal{K}^2_{ee} operator with a target point approaching the surface from the inside

$$\mathcal{K}_{ee}^{2} \mathbf{J} = \hat{n}(\mathbf{r}) \times \int_{S} \overline{\mathbf{G}}_{ee}^{2}(\mathbf{r}, \mathbf{r}') \cdot \mathbf{J}(\mathbf{r}') d\sigma(\mathbf{r}') \Big|_{\mathbf{r} \in S}$$

$$= \hat{n}(\mathbf{r}) \times \int_{S} \overline{\mathbf{G}}_{ee}^{2}(\mathbf{r}, \mathbf{r}') \cdot \mathbf{J}(\mathbf{r}') d\sigma(\mathbf{r}') \Big|_{\mathbf{r} \to \mathbf{r}^{-}}$$

$$= \frac{i\omega\mu_{0}}{4\pi} \hat{n}(\mathbf{r}) \times \int_{S} \left\{ \frac{\nabla\nabla}{\mathbf{k}_{\perp}^{2}} \frac{e^{i\mathbf{k}_{\perp}R_{e}}}{R_{e}} + \overline{\mathbf{D}} \right\} \cdot \mathbf{J}(\mathbf{r}') d\sigma(\mathbf{r}') \Big|_{\mathbf{r} \to \mathbf{r}^{-}}$$

$$= \frac{i\omega\mu_{0}}{4\pi} \hat{n}(\mathbf{r}) \times \left\{ \frac{1}{\mathbf{k}_{\perp}^{2}} \nabla\int_{S} \nabla \frac{e^{i\mathbf{k}_{\perp}R_{e}}}{R_{e}} \cdot \mathbf{J}(\mathbf{r}') d\sigma(\mathbf{r}') + \int_{S} \overline{\mathbf{D}} \cdot \mathbf{J}(\mathbf{r}') d\sigma(\mathbf{r}') \right\} \Big|_{\mathbf{r} \to \mathbf{r}^{-}}$$

$$= \frac{i\omega\mu_{0}}{4\pi} \hat{n}(\mathbf{r}) \times \left\{ \frac{1}{\mathbf{k}_{\perp}^{2}} \nabla\int_{S} \frac{e^{i\mathbf{k}_{\perp}R_{e}}}{R_{e}} \nabla'_{s} \cdot \mathbf{J}(\mathbf{r}') d\sigma(\mathbf{r}') + \int_{S} \overline{\mathbf{D}} \cdot \mathbf{J}(\mathbf{r}') d\sigma(\mathbf{r}') \right\} \Big|_{\mathbf{r} \to \mathbf{r}^{-}}$$

$$+ \int_{S} \overline{\mathbf{D}} \cdot \mathbf{J}(\mathbf{r}') d\sigma(\mathbf{r}') \right\} \Big|_{\mathbf{r} \to \mathbf{r}^{-}}$$
(23)

where

$$\overline{\mathbf{D}} = \epsilon_{\parallel} \frac{e^{i\mathbf{k}_{\perp}\mathbf{R}_{\mathrm{e}}}}{\mathbf{R}_{\mathrm{e}}} \overline{\epsilon}^{-1} - \left[\frac{\epsilon_{\parallel}e^{i\mathbf{k}_{\perp}\mathbf{R}_{\mathrm{e}}}}{\epsilon_{\perp}\mathbf{R}_{\mathrm{e}}} - \frac{e^{i\mathbf{k}_{\perp}\mathbf{R}}}{\mathbf{R}} \right] \left[\frac{(\mathbf{R} \times \hat{\mathbf{c}})(\mathbf{R} \times \hat{\mathbf{c}})}{(\mathbf{R} \times \hat{\mathbf{c}})^{2}} \right]$$

 1 Note: Moving the gradient (∇) outside the integral is not strictly necessary when using the Müller formulation, since its coefficients are designed to cancel the singularity.

$$-\left[\frac{\epsilon_{\parallel} - \epsilon_{\perp}}{\epsilon_{\perp}} \frac{e^{i\mathbf{k}_{\perp}(\mathbf{R}_{e} + \mathbf{R})/2}}{\mathbf{R}_{e} + \mathbf{R}} \frac{\sin\left(\mathbf{k}_{\perp}(\mathbf{R}_{e} - \mathbf{R})/2\right)}{(\mathbf{k}_{\perp}(\mathbf{R}_{e} - \mathbf{R})/2)}\right] \times \left[\bar{\mathbf{I}} - \hat{\mathbf{c}}\hat{\mathbf{c}} - 2\frac{(\mathbf{R} \times \hat{\mathbf{c}})(\mathbf{R} \times \hat{\mathbf{c}})}{(\mathbf{R} \times \hat{\mathbf{c}})^{2}}\right]$$
(24)

and $\mathbf{r} \to \mathbf{r}^-$ indicates that operator is evaluated for a target point that is approaching $\mathbf{r} \in S$ along $-\hat{n}$ from V_2 . Since the kernels of both integrals, $\overline{\mathbf{D}}$ and $e^{i\mathbf{k}_\perp\mathbf{R}_e}/\mathbf{R}_e$, have $O(1/\mathbf{R})$ singularity, the integral operator \mathcal{K}^2_{ee} in this form is weakly singular. \mathcal{K}^2_{mm} , \mathcal{K}^1_{ee} , and \mathcal{K}^1_{mm} can also be readily transformed into weakly singular operators by following the same procedure as \mathcal{K}^2_{ee} .

B. Singularity of $\mathcal{K}_{m_{\theta}}^{2}$

The action of the $\nabla \times$ operator on weakly singular kernels with O(1/R) singularities makes the dyadic Green's functions of the \mathcal{K}_{me}^i and $\mathcal{K}_{em}^i (i \in \{1,2\})$ operators strongly singular with $O(1/R^2)$ -type singularity. Nevertheless, these operators can also be manipulated to become weakly singular when acting on densities by applying vector identities. For example, consider \mathcal{K}_{me}^2 acting on \mathbf{J} , with the target point \mathbf{r} approaching the surface from the inside as before

$$\mathcal{K}_{me}^{2}\mathbf{J} = \hat{n}(\mathbf{r}) \times \int_{S} \overline{\mathbf{G}}_{me}^{2}(\mathbf{r}, \mathbf{r}') \cdot \mathbf{J}(\mathbf{r}') d\sigma(\mathbf{r}') \Big|_{\mathbf{r} \in S} \\
= \hat{n}(\mathbf{r}) \times \int_{S} \overline{\mathbf{G}}_{me}^{2}(\mathbf{r}, \mathbf{r}') \cdot \mathbf{J}(\mathbf{r}') d\sigma(\mathbf{r}') \Big|_{\mathbf{r} \to \mathbf{r}^{-}} + \frac{1}{2}\mathbf{J} \\
= \hat{n}(\mathbf{r}) \times \int_{S} \frac{1}{i\omega\mu_{0}} \nabla \times \overline{\mathbf{G}}_{ee}^{2} \cdot \mathbf{J}(\mathbf{r}') d\sigma(\mathbf{r}') \Big|_{\mathbf{r} \to \mathbf{r}^{-}} + \frac{1}{2}\mathbf{J} \\
= \frac{1}{4\pi} \hat{n}(\mathbf{r}) \times \left\{ \int_{S} \nabla \times \frac{\nabla \nabla}{\mathbf{k}_{\perp}^{2}} \frac{e^{i\mathbf{k}_{\perp}R_{e}}}{R_{e}} \cdot \mathbf{J}(\mathbf{r}') d\sigma(\mathbf{r}') \Big|_{\mathbf{r} \to \mathbf{r}^{-}} \\
+ \int_{S} \nabla \times \overline{\mathbf{D}}(\mathbf{r}, \mathbf{r}') \cdot \mathbf{J}(\mathbf{r}') d\sigma(\mathbf{r}') \Big|_{\mathbf{r} \to \mathbf{r}^{-}} \right\} + \frac{1}{2}\mathbf{J} \\
= \frac{1}{4\pi} \hat{n}(\mathbf{r}) \times \nabla \times \int_{S} \overline{\mathbf{D}}(\mathbf{r}, \mathbf{r}') \cdot \mathbf{J}(\mathbf{r}') d\sigma(\mathbf{r}') \Big|_{\mathbf{r} \to \mathbf{r}^{-}} + \frac{1}{2}\mathbf{J} \\
(25)$$

where $\overline{\mathbf{D}}$ is given in (24), and the second equality follows from the jump condition. Note that the $\nabla\nabla$ term can be removed, since $\nabla\times\nabla\equiv0$. It can be seen that the kernel inside the integral $[\overline{\mathbf{D}}(\mathbf{r},\mathbf{r}')]$ is now weakly singular, since the curl operation has been factored out of the integral. The same procedure can be used to also transform \mathcal{K}^2_{em} , \mathcal{K}^1_{me} , and \mathcal{K}^1_{em} into weakly singular forms.

These operators in their weakly singular form can now be discretized with high-order accuracy using the Chebyshev-based Nyström method that was first introduced in [7] for perfect conductors and isotropic dielectric materials. Section V briefly reviews the key points of the Chebyshev method and discusses our adaptation and application of it to the present anisotropic formulation.

V. Evaluation of Action of Integral Operators $\mathcal{K}^i_{lphaeta}$ Using Chebyshev Expansion-Based Method

According to the analysis in Section IV, two types of weakly singular integrals as well as their gradient and curl need to be

evaluated to compute the action of the integral operators \mathcal{K}^2_{ee} and \mathcal{K}^2_{me} on the current density J

$$\phi(\mathbf{r}) = \int_{S} \frac{e^{i\mathbf{k}_{\perp}R_{e}}}{R_{e}} \nabla_{s}' \cdot \mathbf{J}(\mathbf{r}') d\sigma(\mathbf{r}'), \quad \hat{n}(\mathbf{r}) \times \nabla\phi(\mathbf{r})|_{\mathbf{r}=\mathbf{r}^{-}}$$

$$\mathbf{A}(\mathbf{r}) = \int_{S} \overline{\mathbf{D}}(\mathbf{r}, \mathbf{r}') \cdot \mathbf{J}(\mathbf{r}') d\sigma(\mathbf{r}'), \quad \hat{n}(\mathbf{r}) \times \nabla \times \mathbf{A}(\mathbf{r})|_{\mathbf{r}=\mathbf{r}^{-}}$$
(26)

where $\phi(\mathbf{r})$ and $\mathbf{A}(\mathbf{r})$ are scalar and vector functions of the target point \mathbf{r} , respectively, and $\overline{\mathbf{D}}$ is defined in (24). Note that we focus on the operators acting on \mathbf{J} , since the same procedure can be used to discretize the K_{mm}^2 and K_{em}^2 operators, which act on \mathbf{M} .

A. Evaluation of $\phi(\mathbf{r})$ and $\mathbf{A}(\mathbf{r})$

In order to compute $\phi(\mathbf{r})$ and $\mathbf{A}(\mathbf{r})$, the whole surface S is split into M nonoverlapping curvilinear quadrilateral patches S_p , $p=1,2,\ldots,M$. A parametric mapping is defined from the unit square $[-1,1]\times[-1,1]$ in UV space to each surface S_p in Cartesian coordinates. Specifically, we introduce parameterization $\mathbf{r} = \mathbf{r}^p(u,v) = (x^p(u,v),y^p(u,v),z^p(u,v))$ for patch S_p . The tangential covariant basis vectors and normal vectors on S_p can then be defined as follows:

$$\mathbf{a}_{u}^{p} = \frac{\partial \mathbf{r}^{p}(u, v)}{\partial u}, \ \mathbf{a}_{v}^{p} = \frac{\partial \mathbf{r}^{p}(u, v)}{\partial v}, \ \hat{n}^{p} = \frac{\mathbf{a}_{u}^{p} \times \mathbf{a}_{v}^{p}}{||\mathbf{a}_{v}^{p} \times \mathbf{a}_{v}^{p}||}. \tag{27}$$

The tangential electric current density vector \mathbf{J} on the surface S_p can be expanded in terms of the local tangential coordinate basis as follows:

$$\mathbf{J}^{p}(u,v) = J^{p,u}(u,v)\mathbf{a}_{u}^{p}(u,v) + J^{p,v}(u,v)\mathbf{a}_{v}^{p}(u,v)$$
 (28)

where $\mathbf{J}^p(u, v) \equiv \mathbf{J}(\mathbf{r}^p(u, v))$, and $J^{p,u}$ and $J^{p,v}$ are the contravariant components of the surface current density \mathbf{J} . For sufficiently smooth surface geometries, $J^{p,u}$ and $J^{p,v}$ are smooth functions of u and v and can be approximated with spectral convergence by using Chebyshev polynomials as follows:

$$J^{p,a} = \sum_{m=0}^{N_v^p - 1} \sum_{n=0}^{N_v^p - 1} \gamma_{n,m}^{p,a} T_n(u) T_m(v), \quad \text{for } a = u, v \quad (29)$$

where the Chebyshev coefficients $\gamma_{n,m}^{p,a}$ can be computed from the values of $J^{p,a}$ on S_p at the Chebyshev nodes, which is where the discretized set of unknowns are located, by using the discrete orthogonality property of Chebyshev polynomials

$$\gamma_{n,m}^{p,a} = \frac{\alpha_n \alpha_m}{N_u^p N_v^p} \sum_{k=0}^{N_v^p - 1} \sum_{l=0}^{N_u^p - 1} J^{p,a}(u_l, v_k) T_n(u_l) T_m(v_k). \tag{30}$$

After the Chebyshev coefficients are obtained from the density values on Chebyshev nodes, we are able to compute the density values $J^{p,a}(u,v)$ for arbitrary (u,v) by interpolating via (29), and the Cartesian components $J_i^p(u,v)$ can be computed by taking dot product of Cartesian basis vectors $\mathbf{e}_i(i=x,y,z)$ and $\mathbf{J}^p(u,v)$. Thus, $\phi(\mathbf{r})$ and the *i*th Cartesian component of the integral $\mathbf{A}(\mathbf{r})$ can be represented as follows:

$$\phi(\mathbf{r}) = \sum_{n=1}^{M} \int_{S_p} \frac{e^{i\mathbf{k}_{\perp}\mathbf{R}_e}}{\mathbf{R}_e} \nabla_s' \cdot \mathbf{J}(\mathbf{r}') d\sigma(\mathbf{r}')$$

$$= \sum_{p=1}^{M} \int_{-1}^{1} \int_{-1}^{1} \frac{e^{i\mathbf{k}_{\perp}R_{e}}}{R_{e}} \left(\frac{\partial (\sqrt{|G^{p}|}J^{p,u})}{\partial u} + \frac{\partial (\sqrt{|G^{p}|}J^{p,v})}{\partial v} \right) du dv$$

$$= \sum_{p=1}^{M} \int_{S_{p}} \mathbf{e}_{i} \cdot \overline{\mathbf{D}}(\mathbf{r}, \mathbf{r}') \cdot \mathbf{J}(\mathbf{r}') d\sigma(\mathbf{r}')$$

$$= \sum_{p=1}^{M} \int_{-1}^{1} \int_{-1}^{1} (D_{ix}J_{x}^{p} + D_{iy}J_{y}^{p} + D_{iz}J_{z}^{p}) \sqrt{|G^{p}|} du dv$$
(32)

where $D_{ij} = D_{ij}(\mathbf{r}, \mathbf{r}^p(u, v))(i, j = x, y, z)$ is the Cartesian component of the dyadic $\overline{\mathbf{D}}(\mathbf{r}, \mathbf{r}')$, $J_j^p = J_j^p(u, v)$ is the Cartesian component of current density **J**, and $\sqrt{|G^p|} =$ $\sqrt{|G^p(u,v)|}$ is the surface element Jacobian on the source patch S_p . If the target point **r** is far away from S_p , the kernels D_{ij} and $e^{ik_{\perp}R_e}/R_e$ are smooth, and Fejer's first quadrature rule [23] can be used directly on the discrete densities at the Chebyshev nodes to evaluate the integrals numerically with high-order accuracy. When the target point \mathbf{r} is on the source patch S_p itself or nearby, the integrals become singular or nearly singular and require special treatment. Since the density on each patch can be expanded in terms of a Chebyshev polynomial basis via (29), the action of these integrals on the density J can be computed by first precomputing their action on each Chebyshev basis polynomial, followed by multiplying the resulting values against the expanded Chebyshev coefficients of the density and accumulating over all nand m indices. Since all of the kernels involved have been manipulated to be weakly singular, we adopt the change of variables proposed in [7], [24], and [25, Sec. 3.5] to regularize the integrals by annihilating the singularity with the surface Jacobian, allowing the precomputations to be computed with very high accuracy using a standard Fejer quadrature rule. The Chebyshev discretization and singular integration approaches for the Nyström method are described in depth in [7].

B. Evaluation of $\hat{n}(\mathbf{r}) \times \nabla \phi(\mathbf{r})|_{\mathbf{r}=\mathbf{r}^-}$

In view of the surface representation in terms of nonoverlapping patches, for a target point \mathbf{r} on pth patch S_p , we first expand the ∇ operator in the local coordinate frame as follows:

$$\nabla = \mathbf{a}^{p,u} \frac{\partial}{\partial u} + \mathbf{a}^{p,v} \frac{\partial}{\partial v} + \hat{n}^p \frac{\partial}{\partial \hat{n}^p}$$
 (33)

where $\mathbf{a}^{p,u}$ and $\mathbf{a}^{p,v}$ are contravariant basis vectors that satisfy the orthogonality relation

$$\mathbf{a}^{p,a} \cdot \mathbf{a}_b^p = \begin{cases} 1 & a = b \\ 0 & a \neq b \end{cases}$$
 (34)

The operator can then be expanded as follows:

$$\hat{n}(\mathbf{r}) \times \nabla \phi(\mathbf{r})|_{\mathbf{r} \to \mathbf{r}^{-}}
= \hat{n}^{p} \times \left(\mathbf{a}^{p,u} \frac{\partial \phi}{\partial u} + \mathbf{a}^{p,v} \frac{\partial \phi}{\partial v} + \hat{n}^{p} \frac{\partial \phi}{\partial \hat{n}^{p}} \right) \Big|_{\mathbf{r} \to \mathbf{r}^{-}}
= \frac{\partial \phi}{\partial u} \Big|_{\mathbf{r} \to \mathbf{r}^{-}} \hat{n}^{p} \times \mathbf{a}^{p,u} + \frac{\partial \phi}{\partial v} \Big|_{\mathbf{r} \to \mathbf{r}^{-}} \hat{n}^{p} \times \mathbf{a}^{p,v}
= \frac{\partial \phi}{\partial u} \Big|_{\mathbf{r} \in S_{p}} \hat{n}^{p} \times \mathbf{a}^{p,u} + \frac{\partial \phi}{\partial v} \Big|_{\mathbf{r} \in S_{p}} \hat{n}^{p} \times \mathbf{a}^{p,v}.$$
(35)

Note that the third equality follows from the fact that $\phi(\mathbf{r})$ has continuous tangential derivatives across the surface without any jump condition. As in Section V-A, $\phi(\mathbf{r})$ is first computed at each Chebyshev node (u_l, v_k) on S_p and then expanded with a Chebyshev transform as follows:

$$\phi(\mathbf{r}^{p}(u,v)) = \sum_{m=0}^{N_{v}^{p}-1} \sum_{n=0}^{N_{u}^{p}-1} \zeta_{n,m}^{p} T_{n}(u) T_{m}(v)$$
 (36)

where the values of $\zeta_{n,m}^P$ are the Chebyshev coefficients obtained by using (30) and replacing $J^{p,a}(u_l, v_k)$ with $\phi(\mathbf{r}^p(u_l, v_k))$. The partial derivatives with respect to u and v can then be readily computed by taking the derivatives of Chebyshev polynomials $T_n(u)$ and $T_m(v)$, respectively, as follows:

$$\frac{\partial \phi}{\partial u} \left(\mathbf{r}^p(u, v) \right) = \sum_{m=0}^{N_v^p - 1} \sum_{n=0}^{N_u^p - 1} \zeta_{n,m}^p T_n'(u) T_m(v)$$

$$\frac{\partial \phi}{\partial v} \left(\mathbf{r}^p(u, v) \right) = \sum_{m=0}^{N_v^p - 1} \sum_{n=0}^{N_u^p - 1} \zeta_{n,m}^p T_n(u) T_m'(v) \tag{37}$$

for all target points $\mathbf{r} = \mathbf{r}^p(u, v) \in S_p$, and $\hat{n}(\mathbf{r}) \times \nabla \phi(\mathbf{r})|_{\mathbf{r}=\mathbf{r}^-}$ can then be computed by substituting into expansion (35).

C. Evaluation of $\hat{n}(\mathbf{r}) \times \nabla \times \mathbf{A}(\mathbf{r})|_{\mathbf{r}=\mathbf{r}^{-}}$

By using the same expansion for ∇ operator as in (33), we can expand this operator as follows:

$$\hat{n}(\mathbf{r}) \times \nabla \times \mathbf{A}(\mathbf{r})|_{\mathbf{r} \to \mathbf{r}^{-}} \\
= \hat{n}^{p} \times \left(\mathbf{a}^{p,u} \times \frac{\partial \mathbf{A}}{\partial u} + \mathbf{a}^{p,v} \times \frac{\partial \mathbf{A}}{\partial v} + \hat{n}^{p} \times \frac{\partial \mathbf{A}}{\partial \hat{n}^{p}} \right) \Big|_{\mathbf{r} \to \mathbf{r}^{-}} \\
= \hat{n}^{p} \times \left(\mathbf{a}^{p,u} \times \frac{\partial \mathbf{A}}{\partial u} \Big|_{\mathbf{r} \to \mathbf{r}^{-}} \right) + \hat{n}^{p} \times \left(\mathbf{a}^{p,v} \times \frac{\partial \mathbf{A}}{\partial v} \Big|_{\mathbf{r} \to \mathbf{r}^{-}} \right) \\
+ \hat{n}^{p} \times \left(\hat{n}^{p} \times \frac{\partial \mathbf{A}}{\partial \hat{n}^{p}} \Big|_{\mathbf{r} \to \mathbf{r}^{-}} \right) \\
= \mathbf{a}^{p,u} \left(\hat{n}^{p} \cdot \frac{\partial \mathbf{A}}{\partial u} \Big|_{\mathbf{r} \in S_{p}} \right) + \mathbf{a}^{p,v} \left(\hat{n}^{p} \cdot \frac{\partial \mathbf{A}}{\partial v} \Big|_{\mathbf{r} \in S_{p}} \right) - \frac{\partial \mathbf{A}}{\partial \hat{n}^{p}} \Big|_{\mathbf{r} \to \mathbf{r}^{-}} \\
+ \hat{n}^{p} \left(\hat{n}^{p} \cdot \frac{\partial \mathbf{A}}{\partial \hat{n}^{p}} \Big|_{\mathbf{r} \to \mathbf{r}^{-}} \right) \tag{38}$$

where the tangential derivatives for each Cartesian component of **A**, $\partial \mathbf{A}/\partial u$ and $\partial \mathbf{A}/\partial v$, on S_p can be evaluated in the same way as $\partial \phi/\partial u$ and $\partial \phi/\partial v$ in Section V-B.

According to the limit definition of the directional derivative, the normal derivative of each Cartesian component i of \mathbf{A} , $(\partial \mathbf{A}_i/\partial \hat{n}^p)|_{\mathbf{r}\to\mathbf{r}^-}$, can be written as follows:

$$\frac{\partial \mathbf{A}_{i}}{\partial \hat{n}^{p}}\bigg|_{\mathbf{r} \to \mathbf{r}^{-}} = \lim_{\delta \to 0^{+}} \frac{\mathbf{A}_{i}(\mathbf{r}) - \mathbf{A}_{i}(\mathbf{r} - \delta \hat{n}^{p})}{\delta} \quad i = x, y, z. \quad (39)$$

The normal derivative can be transformed into a derivative of a univariate function by defining auxiliary function, $g(\delta) = A_i(\mathbf{r} + \delta \hat{n}^p)$

$$\frac{\partial \mathbf{A}_{i}}{\partial \hat{n}^{p}}\Big|_{\mathbf{r}=\mathbf{r}^{-}} = \lim_{\delta \to 0^{+}} \frac{\mathbf{A}_{i}(\mathbf{r}) - \mathbf{A}_{i}(\mathbf{r} - \delta \hat{n}^{p})}{\delta}$$

$$= \lim_{\delta \to 0^{+}} \frac{g(0) - g(-\delta)}{\delta} = g'_{-}(0). \tag{40}$$

In order to approximate the derivative $g'_{-}(0)$ numerically with high accuracy without requiring very close off-surface evaluation, we use the following backward difference approximation:

$$\frac{\partial \mathbf{A}_{i}}{\partial \hat{n}^{p}}\Big|_{\mathbf{r}=\mathbf{r}^{-}} = g'_{-}(0) \approx \frac{3g(0) - 4g(-\delta) + g(-2\delta)}{2\delta} \\
= \frac{3\mathbf{A}_{i}(\mathbf{r}) - 4\mathbf{A}_{i}(\mathbf{r} - \delta\hat{n}^{p}) + \mathbf{A}_{i}(\mathbf{r} - 2\delta\hat{n}^{p})}{2\delta} \tag{41}$$

which results in the second-order accuracy $\mathcal{O}(\delta^2)$ as $\delta \to 0^+$. Note that the weakly singular integrals $A_i(\mathbf{r})$, $A_i(\mathbf{r} - \delta \hat{n}^P)$, and $A_i(\mathbf{r} - 2\delta \hat{n}^P)$ in the numerator can be evaluated with high accuracy using the rectangular-singular integration method discussed in Section V-A.

After the two weakly singular integrals $\phi(\mathbf{r})$ and $\mathbf{A}(\mathbf{r})$ and their gradient and curl have been evaluated, respectively, $\mathcal{K}_{ee}^2 \mathbf{J}$ and $\mathcal{K}_{me}^2 \mathbf{J}$ can be obtained by substituting into (23) and (25). The same approach can be used to compute the actions of the other integral operators required, since the kernels of $\mathcal{K}_{mm}^2\mathbf{M}$, $\mathcal{K}_{ee}^{1}\mathbf{J}$, and $\mathcal{K}_{mm}^{1}\mathbf{M}$ are similar to that of $\mathcal{K}_{ee}^{2}\mathbf{J}$, and the kernels of $\mathcal{K}_{em}^{2}\mathbf{M}$, $\mathcal{K}_{me}^{1}\mathbf{J}$, and $\mathcal{K}_{em}^{1}\mathbf{M}$ are similar to that of $\mathcal{K}_{me}^{2}\mathbf{J}$ as discussed in Section IV. Therefore, the LHS of the whole system (22) can be evaluated for an arbitrary target point $\mathbf{r} \in S$. As is done in a typical Nyström method, the operators are evaluated at the same targets points as the unknowns, i.e., at the Chebyshev nodes on each patch, and each equation is tested with the two tangential contravariant basis vectors. This results in a full-rank linear system with the same number of equations as unknowns, which can readily be solved using a suitable linear solver of choice. In this work, we use GMRES to solve the discretized systems iteratively.

VI. NUMERICAL RESULTS

We first study the convergence of the forward map with respect to the number of Chebyshev nodes per side of the patch: $N = N_u^p = N_v^p$ of the forward map. This can be done numerically by applying the whole system (22) operator, which includes the actions of all the integral operators, on reference current densities J and M on a sphere and comparing against an analytical Mie series solution [26]. Following this, we present several examples demonstrating scattering from a uniaxially anisotropic dielectric sphere and cube to highlight the high-order accuracy, which can be achieved with our method. We also solve a scattering example from a 3-D nonuniform rational basis spline (NURBS) model generated by a commercial computer-aided design (CAD) software to demonstrate the ability of our method to handle objects with complicated geometrical features and curvature. Finally, we apply our method to a silicon nanophotonic phase-shifter waveguiding structure and compare the results against a commercial FDTD solver to showcase the potential of our method for simulating nanophotonic devices with high accuracy.

A. Forward Map Convergence

We evaluate convergence of the forward map (application of the integral operator to a prescribed density) on a uniaxially anisotropic dielectric sphere with diameter $D=2\lambda_0$, anisotropic permittivity $\epsilon_{\perp}=2$, $\epsilon_{\parallel}=3$, and distinguished axis $\hat{\mathbf{c}}=(0,0,1)$. Since a refined grid on each patch is used

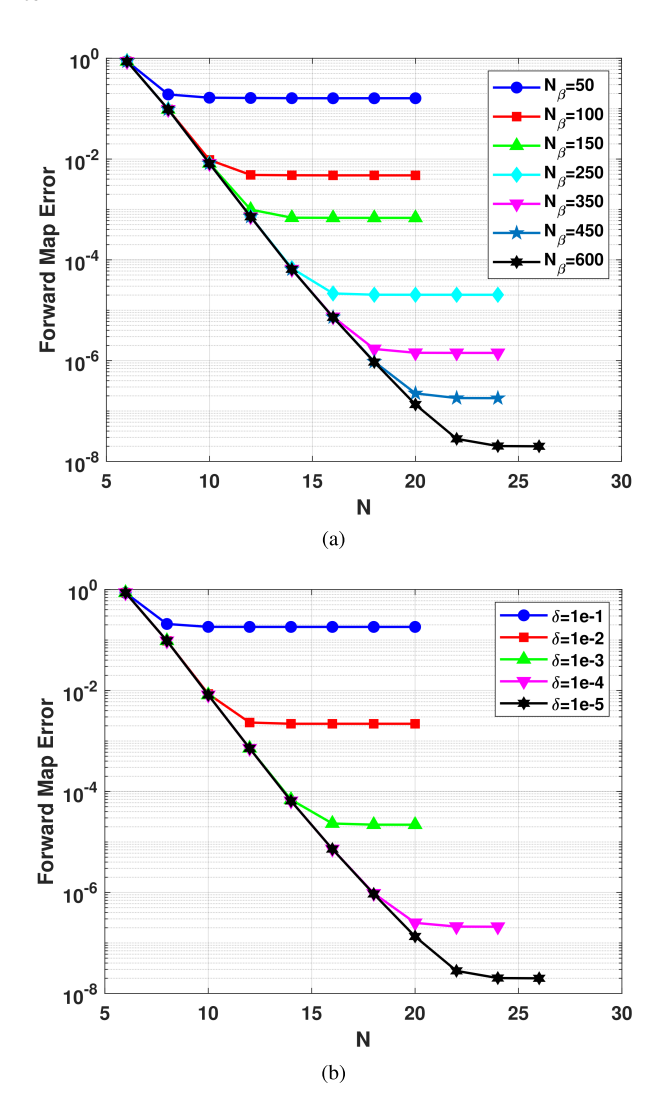


Fig. 2. (a) Forward mapping error with respect to N for different N_{β} values on a uniaxially anisotropic dielectric sphere ($D=2\lambda_0$) with FD step size $\delta=10^{-5}$. (b) Forward mapping error with respect to N for different step sizes δ on the same sphere with $N_{\beta}=600$.

to accurately precompute the action of the integral operator on each Chebyshev polynomial when evaluating the weakly singular integrals, as in [7], the number of refinement grid points $(N_{\beta} \times N_{\beta})$, and the FD step size (δ) in (41), both impact the overall forward map accuracy of the system. In order to study their effect on the convergence, Fig. 2(a) and (b) plots the forward mapping error versus N for increasing N_{β} and decreasing δ in (41), respectively. Note that a sufficiently small $\delta = 10^{-5}$ is used for the plot versus N_{β} , and a sufficiently large $N_{\beta} = 600$ is used for the plot versus δ , such that the convergence is dominated by the parameter that is under consideration in each plot. An analytical Mie series solution for scattering from a uniaxially anisotropic dielectric sphere due to an incident plane wave [26] is used for the reference densities. As expected and discussed in Section V, both the δ and N_{β} parameters affect the overall accuracy significantly and should be chosen judiciously according to the desired overall solution accuracy. Although the curves plotted in Fig. 2 show the forward map convergence of the sphere, they can also be used as guidelines for choosing the N_{β} and δ parameter values to achieve a desired accuracy for different geometrical configurations. For example, choosing $N_{\beta} = 150$ and $\delta = 10^{-3}$ should be suitable for achieving a 10^{-3} relative error.

B. Uniaxially Anisotropic Sphere

Next, we investigate solving the full scattering problem for the same sphere considered in Section VI-A. The electric field of the incident plane wave is given by $\mathbf{E}^{\text{inc}} = \mathbf{e}_x e^{ik_0 z}$. To verify the correctness and accuracy of our results, the result of our solver is compared with the analytical Mie series solution [26].

Fig. 3(a) and (c) shows the magnitudes of electric and magnetic surface current densities, $|\mathbf{J}|$ and $|\mathbf{M}|$, on the sphere for N = 24. In Fig. 3(b) and (d), we plot the associated error of each density on the surface with respect to the analytical solution. Fig. 3(e) compares the RCS for both the E-plane $(\phi = 0^{\circ})$ and H-plane $(\phi = 90^{\circ})$ computed by using a discretization of 12×12 points per patch versus the analytical solution. As can be seen, the results from the solver are indistinguishable from the analytical solution. Fig. 3(f) shows the corresponding relative errors in the solved surface densities concatenated into a single vector [J, M] and the computed RCS far-field in both planes with respect to the analytical solution versus N (number of points per side of each patch), demonstrating the solver's high-order convergence. Note that normalized units $c_0 = \epsilon_0 = \mu_0 = 1$ are used. The relative error of the solved densities for the same sphere with a number of other ϵ_{\perp} and ϵ_{\parallel} configurations, as well as a cube with $1\lambda_0$ side length and high index contrast ($\epsilon_{\perp} = 10$ and $\epsilon_{\parallel} = 20$), is also plotted in Fig. 3(f). Due to lack of an analytical solution, the cube example was compared against a highly refined numerical solution. Although the surface densities of the cube also converge, their rate of convergence is lower than that of the sphere examples, since no particular refinement strategy is used to deal with the edge singularities.

C. Uniaxially Anisotropic Cube

We also consider scattering from a uniaxially aniostropic dielectric cube with $1\lambda_0$ edge length, anisotropic permittivity $\epsilon_\perp=3$, $\epsilon_\parallel=5$, and distinguished axis $\hat{\mathbf{c}}=(1/2,1/2,\sqrt{2}/2)$. The same plane wave incident field is used as the previous example, and the surface of the cube is made up of six patches. Since we are not aware of an analytical solution for this structure, we also compared the result of our solver with a highly refined solution (N=40) as well as with a solution obtained from a commercial FE method (FEM) simulation software.

Fig. 4(a) and (b) shows the magnitudes of the surface electric and magnetic current densities, $|\mathbf{J}|$ and $|\mathbf{M}|$, for N=16. Fig. 4(c) compares the RCS at the E-plane ($\phi=0^{\circ}$) obtained by using a coarse discretization N=16, a highly refined discretization N=40, and the commercial FEM solver ANSYS HFSS [27]. As can be seen, the results from N=16 and N=40 are completely overlapped with each other, demonstrating that the solver has already converged for a relatively coarse discretization, despite the known challenges with objects that have sharp edges and corners that often plague Mawxell solvers. A maximum deviation less than 0.3 dB between our result and the FEM solver result is observed,

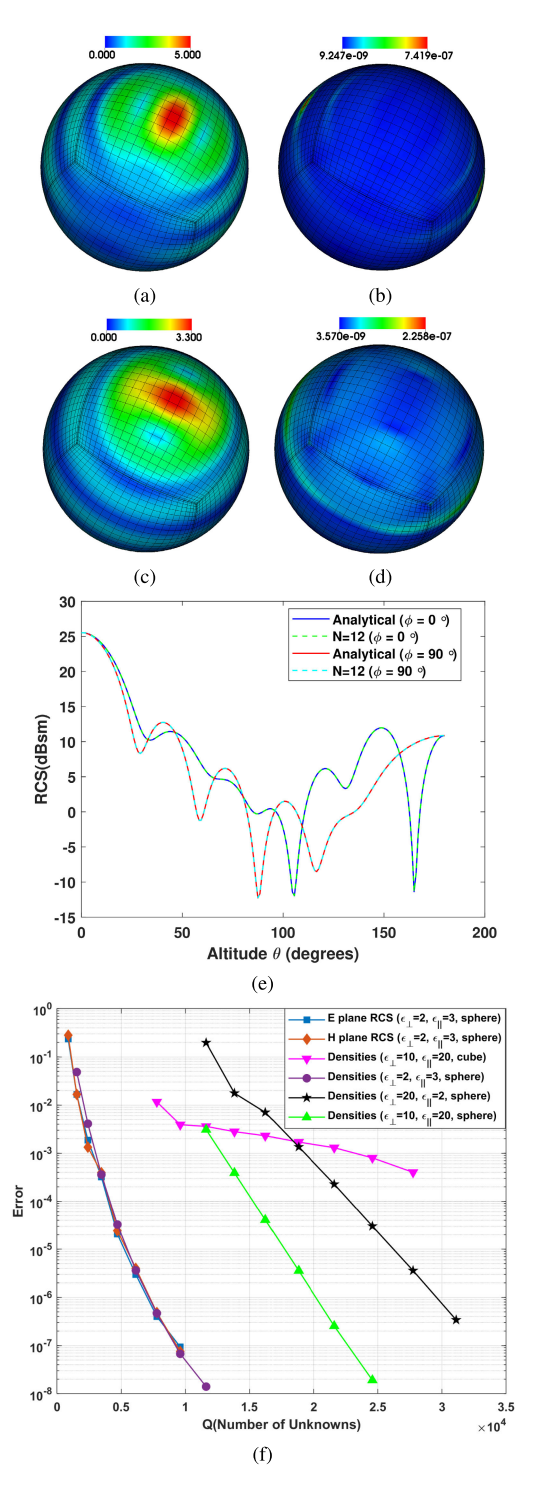


Fig. 3. (a) Magnitude of surface electric current density distribution $|\mathbf{J}|$ on a uniaxially anisotropic dielectric sphere $(D=2\lambda_0)$ induced by incident plane wave. (b) Error of surface $|\mathbf{J}|$ distribution. Max error: 7.4×10^{-7} . (c) Magnitude of surface magnetic current density distribution $|\mathbf{M}|$. (d) Error of surface $|\mathbf{M}|$ distribution. Max error: 2.3×10^{-7} . (e) RCS at E-plane $(\phi=0^\circ)$ and H-plane $(\phi=90^\circ)$ comparing a discretization of N=12 with the exact solution. (f) Far-field relative error for both E- and H-planes and surface density (combined \mathbf{J} and \mathbf{M} vector) relative error for different ϵ configurations, as well as for a $1\lambda_0$ side length cube. The errors in the numerical solutions are compared against analytical Mie series solutions for the sphere examples and against a highly refined numerical solution for the cube. Normalized units $c_0 = \epsilon_0 = \mu_0 = 1$ are used.

which further validates the correctness and effectiveness of our solver for scatters with sharp edges. Note that no particular

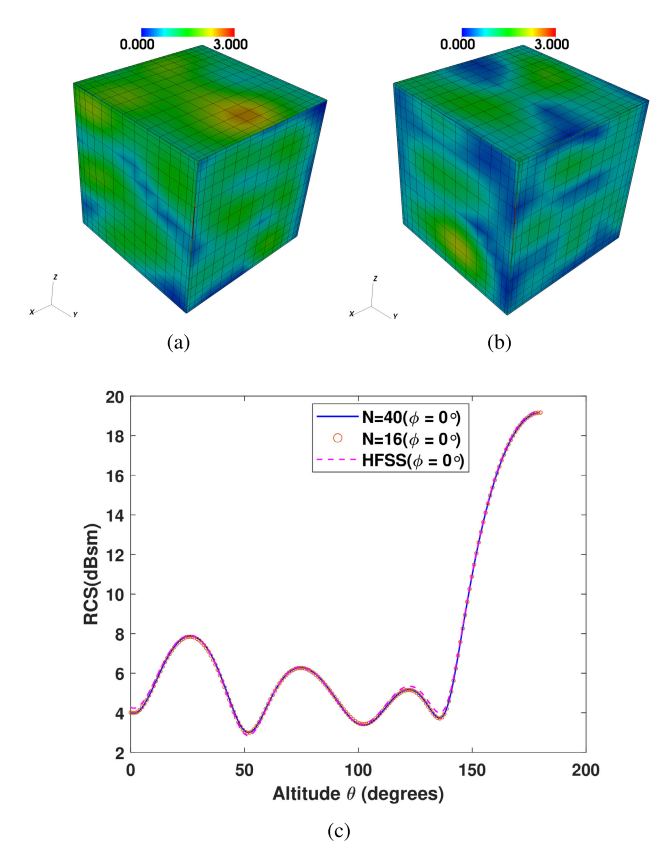


Fig. 4. (a) Magnitude of surface electric current density distribution $|\mathbf{J}|$ on a $1\lambda_0$ edge length uniaxially anisotropic dielectric cube. (b) Magnitude of surface magnetic current density distribution $|\mathbf{M}|$ on the same cube. (c) RCS at E-plane ($\phi=0^{\circ}$) from a coarse discretization N=16, a refined discretization N=40 m, and the commercial FEM solver, ANSYS HFSS.

edge refinement strategy was used in this example, although a similar approach as the edge change of variables used in [7] could be applied to improve the convergence further.

Table I shows the number of GMRES iterations required to reach the relative residual error 10^{-3} versus the number of unknowns Q for various geometry and permittivity settings. It can be seen that the number of iterations remains constant for the cube case and decreases for the two sphere cases as Q increases, indicating that the linear system is well conditioned and does not suffer from dense mesh breakdown.

D. Hummingbird 3-D NURBS CAD Model

We also compute the fields scattered by a hummingbird composed of a uniaxially anisotropic dielectric material. The hummingbird geometry used is a 3-D NURBS CAD model that is available freely online [28]. The same incident excitation and permittivity tensor settings are used as in the sphere example. The hummingbird is sized, such that it has a total length of 4.3 wavelengths and a wingspan of 6.5 wavelengths. This geometry consists of 311 curvilinear quadrilateral patches that were generated by the commercial CAD software Rhino [29].

We plot the magnitude of surface magnetic current density $|\mathbf{M}|$ in Fig. 5(a) and RCS versus θ at $\phi = 0^{\circ}$ for two discretizations N = 10 and N = 12 in Fig. 5(b). The RCS computed using the commercial FE software, ANSYS HFSS [27], is also plotted for comparison. Although this

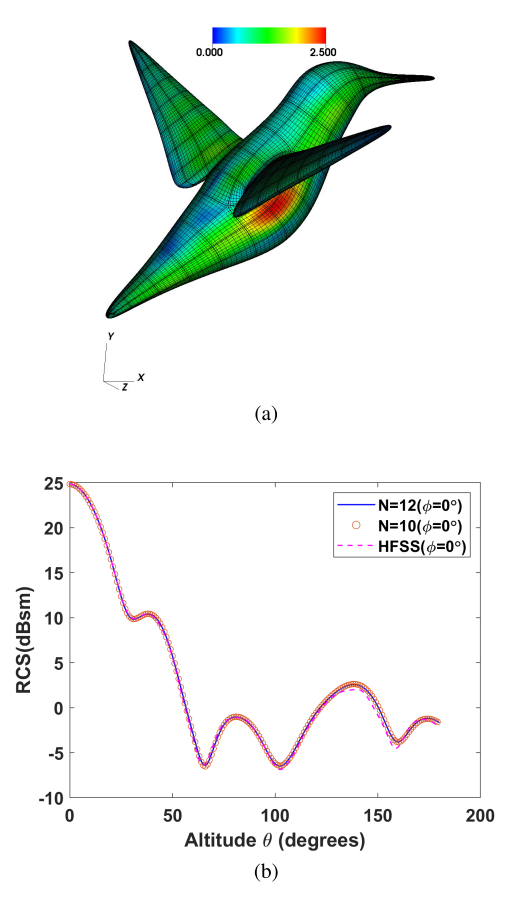


Fig. 5. (a) Magnitude of surface magnetic current density $|\mathbf{M}|$ on a uniaxially anistropic dielectric hummingbird CAD model with surface composed of 311 patches. (b) Comparison of RCS at E-plane ($\phi = 0^{\circ}$) computed using N = 10 and N = 12 discretization orders with the commercial FEM solver ANSYS HFSS.

model contains sharp corners at the beak, tail, and wing tips that could be challenging to simulate accurately, very close agreement is observed for the RCS patterns resulting from the two discretizations and HFSS.

E. Silicon Photonic Phase Shifter

We conclude Section VI with one final example of a silicon-based nanophotonic phase shifter embedded in a liquid crystal background medium. This is a simplified design inspired by Pfeifle et al. [10] and consists of two parallel rectangular silicon waveguides embedded within a uniaxially anisotropic liquid crystal cladding. The orientation of the distinguished axis $\hat{\mathbf{c}}$ of the liquid crystal media can be electrically controlled by an external voltage. By altering the amplitude of this voltage, the distinguished axis is rotated, causing the permittivity experienced by the dominant field component to change and leading to a different corresponding propagation constant. This changes the phase shift experienced by light propagating in the fundamental mode of the waveguide over a certain distance as discussed in [10].

In our example, the width and the height of the rectangular cross sections of both waveguides are 0.24 and 0.22 μ m, respectively, and the spacing between the two silicon rods is 0.12 μ m. The anisotropic permittivity of the liquid crystal cladding is set to be $\epsilon_{\perp}=2.3409$ and $\epsilon_{\parallel}=2.9241$, the

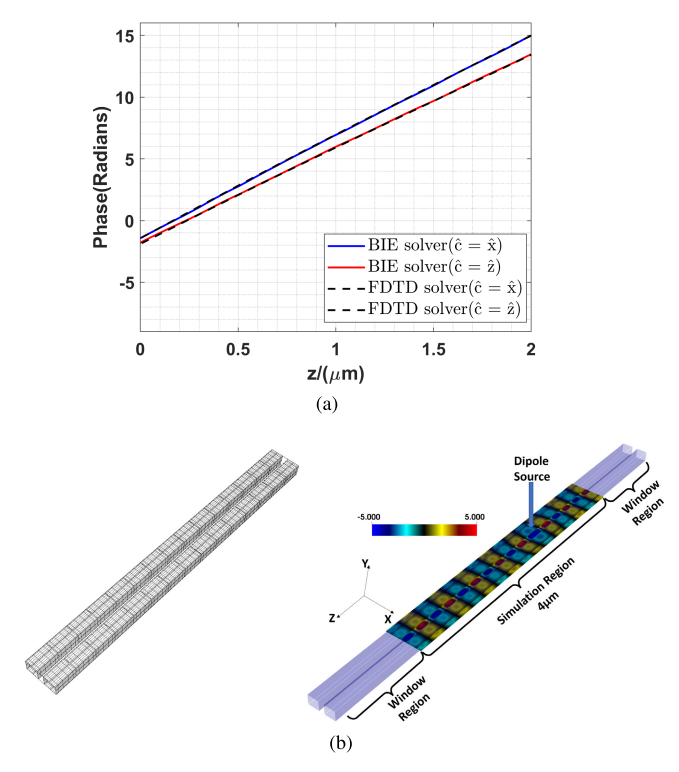


Fig. 6. (a) Phase variation of E_x along the propagation direction for both $\hat{\mathbf{c}} = \hat{\mathbf{x}}$ and $\hat{\mathbf{c}} = \hat{\mathbf{z}}$. (b) Real part of E_x on the planar cross section $-0.4~\mu\mathrm{m} \le x \le 0.4~\mu\mathrm{m}$ and $-2~\mu\mathrm{m} \le z \le 2~\mu\mathrm{m}$.

distinguished axis $\hat{\mathbf{c}}$ is set to either $\hat{\mathbf{x}}$ or $\hat{\mathbf{z}}$, and the silicon waveguide has permittivity $\epsilon_{\rm Si}=12.11$. We use an electric dipole polarized along (1,0,0) direction with unit amplitude and 1.55 μ m free space wavelength placed at (0,0,-1) as the source excitation. The windowed Green function (WGF) method is used to simulate the waveguides extending into infinity from both directions [3], [5], [6].

Fig. 6(a) shows the phase variation of the dominant field component E_x along the propagation direction for both $\hat{\mathbf{c}} = \hat{\mathbf{x}}$ and $\hat{\mathbf{c}} = \hat{\mathbf{z}}$ obtained by using our solver as well as a commercial FDTD solver. The results of the two solvers match very closely with each other. As expected, due to the difference in the propagation constants of the propagating modes caused by rotating the distinguished axis of the liquid crystal cladding from $\hat{\mathbf{c}} = \hat{\mathbf{x}}$ to $\hat{\mathbf{c}} = \hat{\mathbf{z}}$, the slopes of the phase versus position for the two scenarios are different. The discretization mesh is shown on the left side of Fig. 6(b), and the real part of the E_x field on the planar cross section $-0.4~\mu m \le x \le 0.4~\mu m$, $-2~\mu m \le z \le 2~\mu m$ is depicted on the right, indicating single mode propagation along the waveguide.

VII. CONCLUSION

We introduced a high-order accurate approach to solve the 3-D Maxwell surface integral equation (SIE) formulation for scattering from uniaxially anisotropic objects and media. Specifically, we utilized vector identities to represent the integral operators in terms of weakly singular integrals and their gradients and curls. A Chebyshev polynomial expansion-based approach similar to the one used in our previous work for isotropic dielectric and metallic objects [7] is applied for discretizing and evaluating these operators numerically. The high accuracy of the method is verified by comparing the convergence of the solution for scattering from a uniaxial anisotropic dielectric sphere to an analytical solution. Other examples were also presented, including scattering from a uniaxially anisotropic cube, a 3-D NURBS model generated by a commercial CAD software, and a silicon photonic phase shifter embedded in a liquid crystal background medium, which demonstrate the effectiveness and versatility of the solver for handling many different scenarios. Future work includes using the solver to inverse design high-performance radio-frequency and nanophotonic devices using uniaxially anisotropic materials, such as liquid crystals, which can be dynamically reconfigured by switching their polarization states.

REFERENCES

- S. Makarov, "MoM antenna simulations, with MATLAB: RWG basis functions," *IEEE Antennas Propag. Mag.*, vol. 43, no. 5, pp. 100–107, Oct. 2001
- [2] P. Yla-Oijala and M. Taskinen, "Application of combined field integral equation for electromagnetic scattering by dielectric and composite objects," *IEEE Trans. Antennas Propag.*, vol. 53, no. 3, pp. 1168–1173, May 2005.
- [3] C. Sideris, E. Garza, and O. P. Bruno, "Ultrafast simulation and optimization of nanophotonic devices with integral equation methods," *ACS Photon.*, vol. 6, no. 12, pp. 3233–3240, 2019.
- [4] E. Garza, J. Hu, and C. Sideris, "High-order Chebyshev-based Nyström methods for electromagnetics," in *Proc. Int. Appl. Comput. Electromagn. Soc. Symp. (ACES)*, Aug. 2021, pp. 1–4.
- [5] E. Garza, C. Sideris, and O. P. Bruno, "A boundary integral method for 3D nonuniform dielectric waveguide problems via the windowed green function," 2021, arXiv:2110.11419.
- [6] O. P. Bruno, E. Garza, and C. Perez-Arancibia, "Windowed green function method for nonuniform open-waveguide problems," *IEEE Trans. Antennas Propag.*, vol. 65, no. 9, pp. 4684–4692, Sep. 2017.
- [7] J. Hu, E. Garza, and C. Sideris, "A Chebyshev-based high-order-accurate integral equation solver for Maxwell's equations," *IEEE Trans. Antennas Propag.*, vol. 69, no. 9, pp. 5790–5800, Sep. 2021.
- [8] D. Pozar, "Radiation and scattering from a microstrip patch on a uniaxial substrate," *IEEE Trans. Antennas Propag.*, vol. AP-35, no. 6, pp. 613–621, Jun. 1987.
- [9] G. Mumcu, K. Sertel, J. L. Volakis, I. Vitebskiy, and A. Figotin, "RF propagation in finite thickness unidirectional magnetic photonic crystals," *IEEE Trans. Antennas Propag.*, vol. 53, no. 12, pp. 4026–4034, Dec. 2005.
- [10] J. Pfeifle, L. Alloatti, W. Freude, J. Leuthold, and C. Koos, "Siliconorganic hybrid phase shifter based on a slot waveguide with a liquid-crystal cladding," *Opt. Exp.*, vol. 20, pp. 15359–15376, Jun. 2012.
- [11] G. Mumcu, K. Sertel, and J. L. Volakis, "Surface integral equation solutions for modeling 3-D uniaxial media using closed-form dyadic Green's functions," *IEEE Trans. Antennas Propag.*, vol. 56, no. 8, pp. 2381–2388, Aug. 2008.
- [12] Y. Shi and J.-M. Jin, "Scattering analysis of mixed metallic/uniaxial objects using surface integral equations accelerated by adaptive cross approximation algorithm," in *Proc. IEEE Antennas Propag. Soc. Int.* Symp., Jul. 2010, pp. 1–4.
- [13] C. Lv, Y. Shi, and C.-H. Liang, "Higher order hierarchical legendre basis functions application to the analysis of scattering by uniaxial anisotropic objects," *Prog. Electromagn. Res. M*, vol. 13, pp. 133–143, 2010.
- [14] C.-J. Lv, J. Qing, Y. Shi, L. Li, and C.-H. Liang, "Analysis of scattering by an anisotropic uniaxial-coated conducting sphere using higher order hierarchical MoM," in *Proc. Int. Symp. Signals, Syst. Electron.*, Sep. 2010, pp. 1–4.
- [15] Y. Shi and C.-H. Liang, "Analysis of uniaxial media using Calderónpreconditioned single-source combined field integral equation," *IEEE Antennas Wireless Propag. Lett.*, vol. 13, pp. 491–494, 2014.
- [16] W. S. Weiglhofer, "Dyadic Green's functions for general uniaxial media," *IEE Proc. H-Microw., Antennas Propag.*, vol. 137, no. 1, pp. 5–10, 1990.

- [17] A. Poggio and E. Miller, "Computer techniques for electromagnetics," in Integral Equation Solutions for Three Dimensional Scattering Problems. Oxford, U.K.: Pergamon, 1973.
- [18] Y. Chang and R. F. Harrington, "A surface formulation for characteristic modes of material bodies," *IEEE Trans. Antennas Propag.*, vol. AP-25, no. 6, pp. 789–795, Nov. 1977.
- [19] T.-K. Wu and L. L. Tsai, "Scattering from arbitrarily-shaped lossy dielectric bodies of revolution," *Radio Sci.*, vol. 12, no. 5, pp. 709–718, Sep./Oct. 1977.
- [20] S. M. Rao, D. R. Wilton, and A. W. Glisson, "Electromagnetic scattering by surfaces of arbitrary shape," *IEEE Trans. Antennas Propag.*, vol. AP-30, no. 3, pp. 409–418, May 1982.
- [21] P. Yla-Oijala and M. Taskinen, "Calculation of CFIE impedance matrix elements with RWG and n× RWG functions," *IEEE Trans. Antennas Propag.*, vol. 51, no. 8, pp. 1837–1846, Aug. 2003.
- [22] P. Ylä-Oijala and M. Taskinen, "Well-conditioned Müller formulation for electromagnetic scattering by dielectric objects," *IEEE Trans. Antennas Propag.*, vol. 53, no. 10, pp. 3316–3323, Oct. 2005.
- [23] J. Waldvogel, "Fast construction of the Fejér and Clenshaw-Curtis quadrature rules," BIT Numer. Math., vol. 46, no. 1, pp. 195–202, 2006.
- [24] O. P. Bruno and E. Garza, "A Chebyshev-based rectangular-polar integral solver for scattering by geometries described by non-overlapping patches," *J. Comput. Phys.*, vol. 421, Nov. 2020, Art. no. 109740.
- [25] D. L. Colton and R. Kress, Inverse Acoustic and Electromagnetic Scattering Theory, 3rd ed. Berlin, Germany: Springer, 2013.
- [26] Y.-L. Geng, X.-B. Wu, L.-W. Li, and B.-R. Guan, "Mie scattering by a uniaxial anisotropic sphere," *Phys. Rev. E, Stat. Phys. Plasmas Fluids Relat. Interdiscip. Top.*, vol. 70, no. 5, Nov. 2004, Art. no. 056609.
- [27] Ansys HFSS. Accessed: Mar. 2022. [Online]. Available: https://www.ansys.com/products/electronics/ansys-hfss
- [28] Hummingbird From Grab CAD. Accessed: Mar. 2022. [Online]. Available: https://grabcad.com/library/hummingbird-8
- [29] Robert McNeel & Associates. Rhino3D. Accessed: Mar. 2022. [Online]. Available: https://www.rhino3d.com/



Jin Hu (Graduate Student Member, IEEE) received the B.Eng. degree in electronic information engineering from the University of Science and Technology of China, Hefei, China, in 2016, and the M.S. degree in electrical engineering from the University of Southern California, Los Angeles, CA, USA, in 2019, where he is currently pursuing the Ph.D. degree with the Ming Hsieh Department of Electrical and Computer Engineering.

His research interests include boundary integral equation methods for electromagnetics scattering

analysis and their applications for simulation and design of nanophotonic devices.



Constantine Sideris (Member, IEEE) received the B.S., M.S., and Ph.D. degrees (Hons.) from the California Institute of Technology (Caltech), Pasadena, CA, USA, in 2010, 2011, and 2017, respectively.

He was a Visiting Scholar with the Berkeley Wireless Research Center, Berkeley, CA, USA, from 2013 to 2014. He was a Post-Doctoral Scholar with the Department of Computing and Mathematical Sciences, Caltech, from 2017 to 2018, working on integral equation methods for

electromagnetics. He is currently an Assistant Professor of electrical and computer engineering with the University of Southern California, Los Angeles, CA, USA. His research interests include RF and millimeter-wave integrated circuits for bioelectronics and wireless communications, applied electromagnetics, and computational electromagnetics for antenna design and nanophotonics.

Dr. Sideris was a recipient of the Office of Naval Research (ONR) YIP Award in 2023, the NSF CAREER Award in 2021, the Air Force Office of Scientific Research (AFOSR) YIP Award in 2020, the Caltech Leadership Award in 2017, and the NSF Graduate Research Fellowship in 2010.